The Impact of Pressure Gradient History on Flow Structures in High Reynolds Number Rough Wall Turbulence

T. Preskett, B. Ganapathisubramani July 9, 2025

Abstract

High Reynolds number experiments are conducted over a rough wall with strong non-equilibrium pressure gradients. The boundary layer is exposed to different pressure gradient histories via an aerofoil mounted above the boundary layer. Particle image velocity (PIV) allows for the flow development from one chord upstream of the leading edge to one chord downstream of the trailing edge to be captured (3.75m or $\approx 22\delta_0$). The freestream speed upstream of the aerofoil is set to 20 m/s, and the resulting Re_{τ} varies from 12900 to 18500. The integral pressure gradient history parameter is seen to have a second-order relationship with the wake strength, Π . Furthermore, the extent to which the upstream history has to be accounted for is considered. The structures within the flow are examined first through the mean turbulence intensity profiles as well as quadrant analysis. These results show that the effect of flow events on adverse and favourable pressure gradients varies depending on the position within the boundary layer. Some success is achieved in matching the turbulence profiles and flow structure length scales through the integral of the pressure gradient history. The agreement is improved for cases where the local pressure gradient history parameter is also matched.

1 Introduction

High Reynolds number turbulent boundary layers (TBLs) are prevalent in modern engineering applications. Since these TBLs frequently develop over rough surfaces, understanding flow behaviour over roughness has become a topic of significant interest. The reviews of rough wall studies have been covered extensively by Jiménez (2004) and more recently Chung et al. (2021). A rough wall TBL is often represented by the composite log-wake profile given by equation 1. This profile describes the variation in the mean streamwise velocity (U) with varying wall normal position (y).

$$U_{rough}^{+} = \frac{1}{\kappa} ln \left(\frac{y - d}{y_0} \right) + \frac{\Pi}{\kappa} W(\eta) \text{ with, } \eta = \frac{y - d}{\delta - d}$$
 (1)

where $U^+ = U/U_\tau$ is the mean velocity scaled with skin friction velocity $(U_\tau = \sqrt{\tau_w/\rho}, \tau_w)$ is the wall-shear-stress and ρ is the fluid density), $y^+ = yU_\tau/\nu$ is the inner scaled wall-normal position (ν is the kinematic viscosity), κ and B are von Kármán constant and smooth wall intercept. For this work, κ and B are assumed to be 0.39 and 4.3, respectively, as given in Marusic et al. (2013). y_0 represents the drag due to a given rough wall and is related to the equivalent sand grain roughness (k_s) as defined by Nikuradse (1933) (Chung et al. (2021)). d represents the virtual origin of the log layer and is again a property of the flow and surface conditions. The outer region of the flow beyond the log region, where the cut-off is often taken to be 0.15 δ (Jiménez (2004); Monty et al. (2011); Chung et al. (2021)), is dominated by Cole's wake strength, Π . The wake function W has assumed many forms in previous work, often a sin function or polynomial being used (Coles (1956); Lewkowicz (1982)).

While previous studies and reviews have predominantly focused on zero pressure gradient (ZPG) flows, many engineering applications involve varying pressure gradients (PGs) and surface perturbations. A recent review by Devenport and Lowe (2022) gives a detailed look at the previous studies of both equilibrium and non-equilibrium studies. When considering PG flows, the parameter most chosen to represent the PG conditions is the Rota-Clauser

^{*}tdp1g17@soton.ac.uk

parameter, β , originally defined by Clauser (1954). β is given by equation 2 where δ^* is the displacement thickness, τ_w is the wall shear stress and dP/dx the local pressure gradient.

$$\beta = \frac{\delta^*}{\tau_w} \frac{dP}{dx} \tag{2}$$

The work of Monty et al. (2011) presented a parametric study to decouple the effect of PG and Reynolds number. Their work shows a clear effect on the wake and log region caused by the different local PG conditions. It was seen that an APG leads to a larger wake and reduces the length of the log law. For FPG flows, such as those in Tay et al. (2009) and Volino (2020), the FPG reduces wake strengths and leads to thinner boundary layers. Furthermore, APGs have been seen to result in a reduction in skin friction, while FPG results in an increase for a rough wall flow (Shin and Song (2015a,b); Volino (2020)). These studies can all be described as being non-equilibrium boundary layers; these are ones in which $\beta \neq constant$ (Monty et al. (2011)). Bobke et al. (2017) presented LES (Large Eddy Simulation) data with a range of different β histories. Their work demonstrated that up to 7δ of development is required with a similar β history for no differences to be observed in turbulent profiles. Vinuesa et al. (2017) extended this work and the understanding of PG history effects, aiming to capture the accumulated history effects using $\overline{\beta}$, which is a product of the integral of the β history. Recent work by authors, Preskett et al. (2025), has shown that the integral of the PG could be used to predict the local skin friction and boundary layer properties. This work gave higher weighting to PG history nearer to the point of interest using a linear weighting function. When calculating the integral of the PG, all available upstream data was considered. However, it is unclear what the optimum integration length is; this is the amount of upstream history that is needed to capture the trends in the flow.

Previous studies have also explored the effects of pressure gradients on the flow structures. Mean turbulence profiles have been seen to show clear PG history effects. For an APG, a commonly observed outcome on both smooth and rough walls is the development of an outer peak in the streamwise turbulence profiles, $\overline{u}\overline{u}$ (Krogstad and Skåre (1995); Tsikata and Tachie (2013)). This peak is clearer to see when inner scaling is used, although is also seen with outer scaling as seen in Monty et al. (2009). In cases of large APGs, this outer peak can surpass the strength of the inner peak. Studies such as Monty et al. (2011), Lee (2017), and Sanmiguel Vila et al. (2020) attribute this pronounced outer peak to the increased energy of large-scale outer structures compared to ZPG conditions. The laser Doppler velocimetry (LDV) of Volino (2020) showed a reduction in the outer region when inner scaling is used due to an FPG for a smooth wall. When outer scaling is used, Shin and Song (2015b) saw an increase in the outer region $\overline{u}\overline{u}$ profile; an increase in the near wall region was also seen.

The turbulent events contributing to Reynolds stress can be categorised into four types, referred to as Q1–Q4 events. The primary contributors to the overall \overline{wv} are Q2 and Q4 events, known as ejection and sweep events. Sweep events involve the movement of high-speed fluid towards the wall, while ejection events involve the movement of low-speed fluid away from the wall. Planar PIV data from Volino (2020) and Volino and Schultz (2023) indicated that ejection events are less significant near the wall under APG conditions. In contrast, for FPG conditions, the significance of sweep events in the near-wall region is reduced compared to ejection events. Their work also looked into the effect of length scales and the inclination of the structures within the flow. FPGs were observed to reduce the inclination while increasing the streamwise length scale of the structures. Conversely, APGs had the opposite effect, increasing the inclination and reducing the streamwise length scale. However, how rapidly changing pressure gradient histories affect the flow structures is still not fully understood. Volino (2020) and Volino and Schultz (2023) suggested that the near-wall flows respond faster to changes in PG than the outer region based on both C_f and flow structure observations. This has been seen over both smooth and rough wall flows.

The present study aims to explore some of the above-mentioned open questions. A NACA0012 aerofoil imposes rapidly changing pressure gradients on a turbulent boundary layer over a rough wall. Planar PIV measurements are obtained from one chord upstream to one chord downstream of the aerofoil to allow the effect on the rough wall TBL to be seen. This work focuses on the effects of pressure gradient over a single rough wall and therefore focuses only on the differences caused by pressure gradients. We specifically aim to address the following questions: (i) What is the optimum integration length required to capture the non-equilibrium effects on the mean flow? (ii) Are the matched history conditions enough to capture the effect on turbulence profiles? (iii) How do different PG histories and roughness combine to affect the length scales within the flow?

2 Methodology

Experiments were conducted in the University of Southampton's boundary layer wind tunnel, which has dimensions of $1.2 \text{ m} \times 1.0 \text{ m} \times 12 \text{ m}$ (W×H×L) and is equipped with a heat exchanger for maintaining constant conditions. A NACA0012 aerofoil with a chord (c) of 1.25 m was mounted on four actuators attached to the tunnel roof to generate

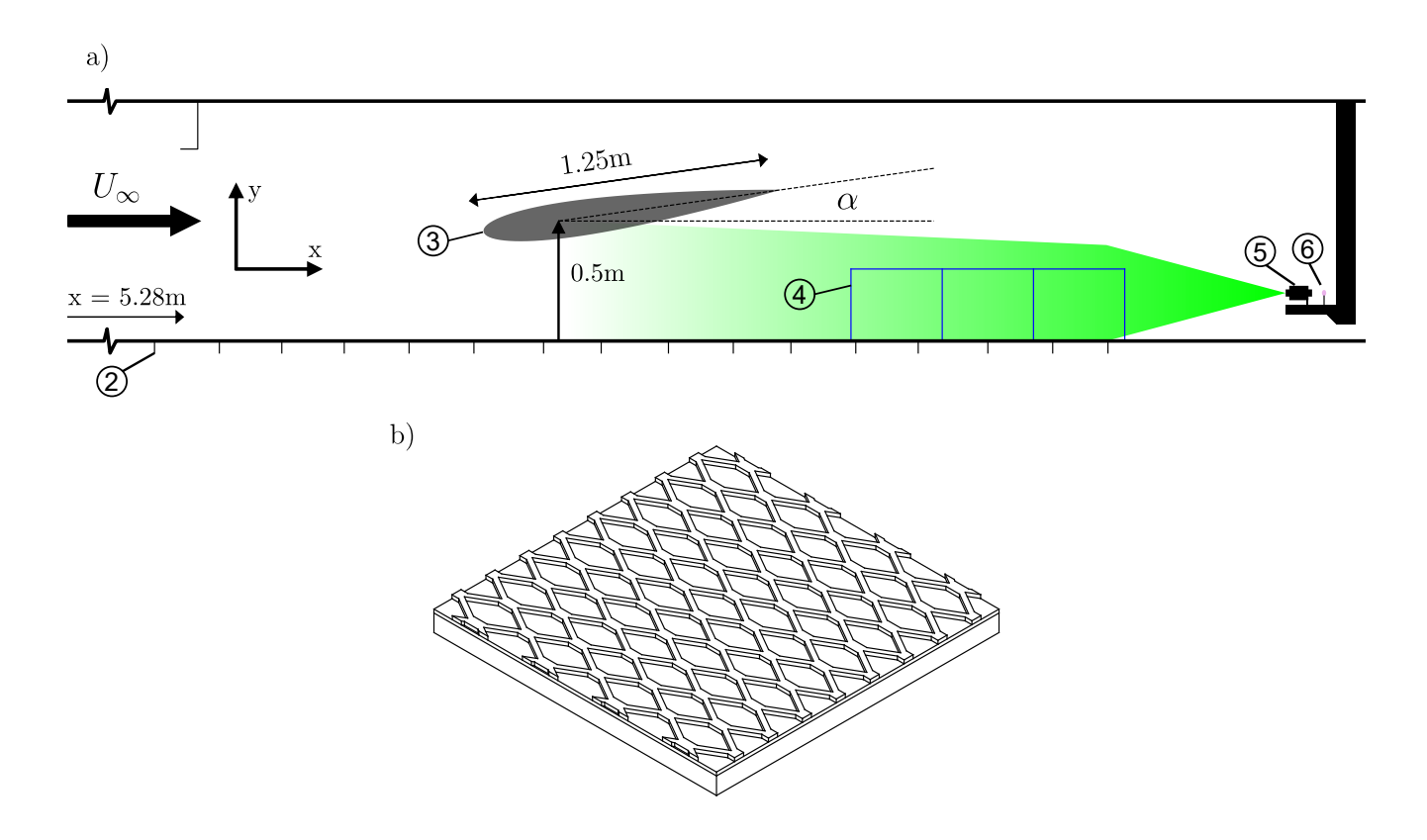


Figure 1: (a) Diagram showing the simplified experimental setup for obtaining PIV flow fields. ① shows the pitot tube mounted at 5.28m from the start of the test section, ② shows the position of the 16 wall pressure taps, ③ shows the NACA0012 aerofoil mounted 6.53m from the test section start, ④ shows field of view of the three cameras for one position, ⑤ shows the beam optics used to focus and produce the laser sheet and ⑥ shows the mirror used to reflect the light within the tunnel. α is the angle of attack of the aerofoil. (b) Cutout of rough wall surface used during the experiment showing the 3mm chicken wire mounted on top of an acrylic wall.

different pressure gradient histories. The aerofoil was positioned at five angles of attack, ranging from -8° to 8° in 4° increments. Its pivot point was located at 0.25c, 500 mm above the tunnel floor, with the leading edge placed 6.5 m downstream of the tunnel inlet. A simplified diagram of this setup is shown in figure 1a. The rough wall beneath the aerofoil consisted of chicken wire type mesh mounted on an acrylic wall shown in figure 1b. The mesh has an open area of 73% and is formed from diamond-shaped elements. Each element has dimensions of 62x30 mm and is oriented such that the longest dimension is in the spanwise direction and the shortest in the streamwise direction. The mesh elements have a width of 4 mm with a height, k, of 3 mm.

Particle Image Velocimetry (PIV) captured the flow history from one chord upstream of the aerofoil's leading edge to one chord downstream of its trailing edge. The region of interest was divided into four sections to ensure adequate magnification. This study focuses on outer flow structures, so high near-wall resolution was not required. Due to laser reflections caused by the roughness elements' sharp edges, the first velocity vector is, on average, located 3k from the underlying smooth wall. This corresponds to between 0.03δ to 0.08δ , depending on the position within the domain, since δ varies with PG. Three LaVision ImagerProLX 16MP cameras with Sigma 105 mm f2.8 lenses were used at each position, achieving an average magnification of 10.9 pix/mm and a field of view of $0.44 \text{ m} \times 0.30 \text{ m}$ (L×H) per camera. The stitched field of view for each position was approximately $1.2 \text{ m} \times 0.3 \text{ m}$. At each position, 2000 instantaneous snapshots were collected for statistical convergence. Images were acquired at 0.5 Hz, ensuring uncorrelated snapshots. The laser sheet, generated by a Litron Bernoulli 200-15 Nd:YAG laser (532 nm wavelength) and LaVision sheet optics, was aligned downstream of the measurement area, as shown in figure 1. All measurements were taken at a freestream velocity of 20 m/s, calibrated using a pitot tube located one chord upstream of the aerofoil. Symbols and line styles used for plotting are shown in table 1. Nominally, symbols will be used for discrete data points, while lines will be used when showing continuous data, such as variation in properties from PIV.

The pressure gradient history was determined using 16 pressure taps along the tunnel floor (indicated by vertical

	-8°	-4°	0°	4°	8°
Symbol		_	•	A	•
Line					

Table 1: The colours used for each angle of attack (α) throughout this paper. The markers are used for data points, while lines of the same colours will be used for PIV data

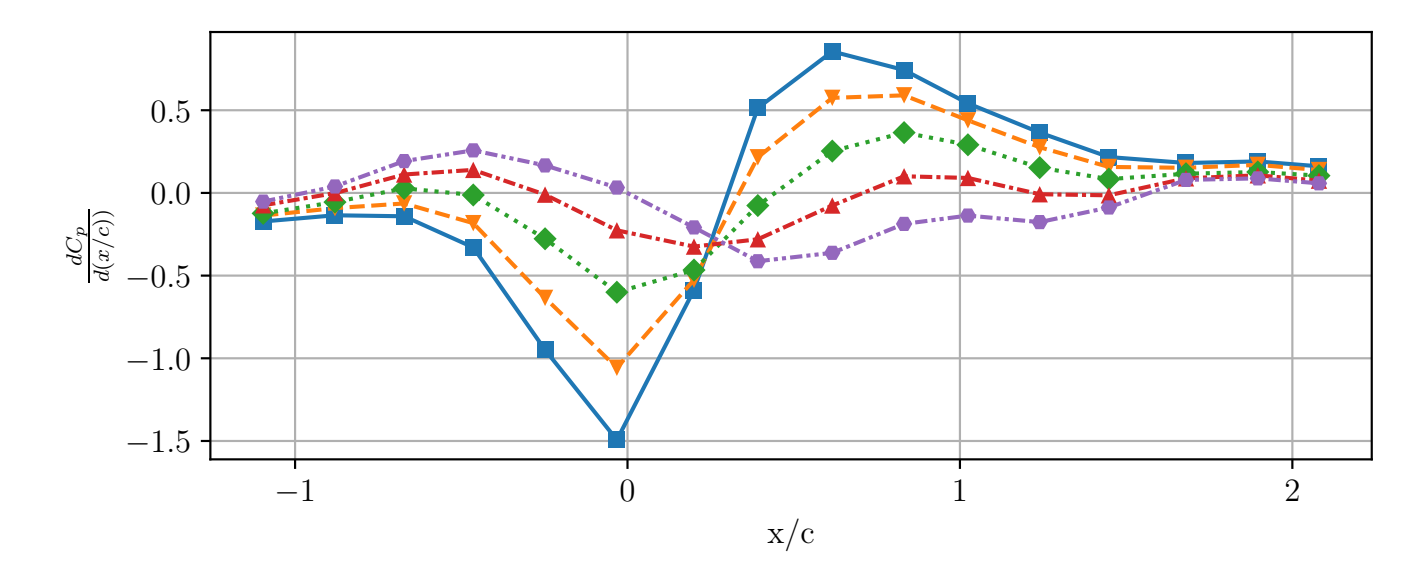


Figure 2: Mean pressure coefficient gradient with respect to x/c $(dC_p/d(x/c))$ for the five angles of attack. The data points are direct from the pressure scanner and the lines for illustrative purposes only. Symbols and linestyles as given in table 1

lines in figure 1). The taps were spaced approximately 0.26 m apart (adjusted for roughness elements and tunnel structure) and were connected to a ZOC 33/64 pressure scanner. This configuration captured the mean pressure distribution from one chord upstream to one chord downstream of the aerofoil. The uncertainty in C_p at a 95% confidence interval is 0.027. Figure 2 shows the mean pressure gradient as calculated from the mean pressure distribution. Firstly, at x/c = 0.25, there is a crossover point due to the aerofoil being rotated around this point. It can be seen that there are two case types: those that experience an FPG and then APG (-8° , -4° and 0°) and those that experience an APG and then FPG (4° and 8°). As can be seen, there is close to zero pressure gradient, one chord upstream of the leading edge and one chord downstream of the trailing edge. Examination of the variation of the wall pressure shows that the flow is attached and stable. This conclusion is reached by the maximum standard deviation of all cases being very similar. Similarly, comparison of HWA data and PIV data at different streamwise measurement stations shows the flow to be spanwise uniform in the middle 3rd of the tunnel outside of the wall effects. Between these two points, varying pressure gradient histories allow for the examination of the change in flow properties and structures. Further comparison of the velocity profiles between the HWA and PIV profiles is given in Appendix A.

3 Mean Flow Fields and Flow History

To understand the flow structures, it is essential first to examine the mean flow fields and the history experienced by the flow. The mean streamwise flow fields (U/U_{∞}) are shown in figure 3 along with the black dashed line showing the boundary layer edge. The boundary layer thickness, δ , and corresponding boundary layer edge velocity, U_{99} , are found using the method based on the local turbulence intensity as set out in Vinuesa et al. (2016). A threshold of $\overline{u}/(U\sqrt{H}) < 0.02$ is used, where \overline{u} is the root mean square of U, U is the local mean velocity, and H is the local shape factor. The reason for this and not using conventional methods is due to the lack of conventional freestream flow. Typically, the flow outside the boundary layer remains at a constant speed. However, the wing leads to a constantly changing freestream. Take figure 3a, the freestream speed continues to increase under the wing in the

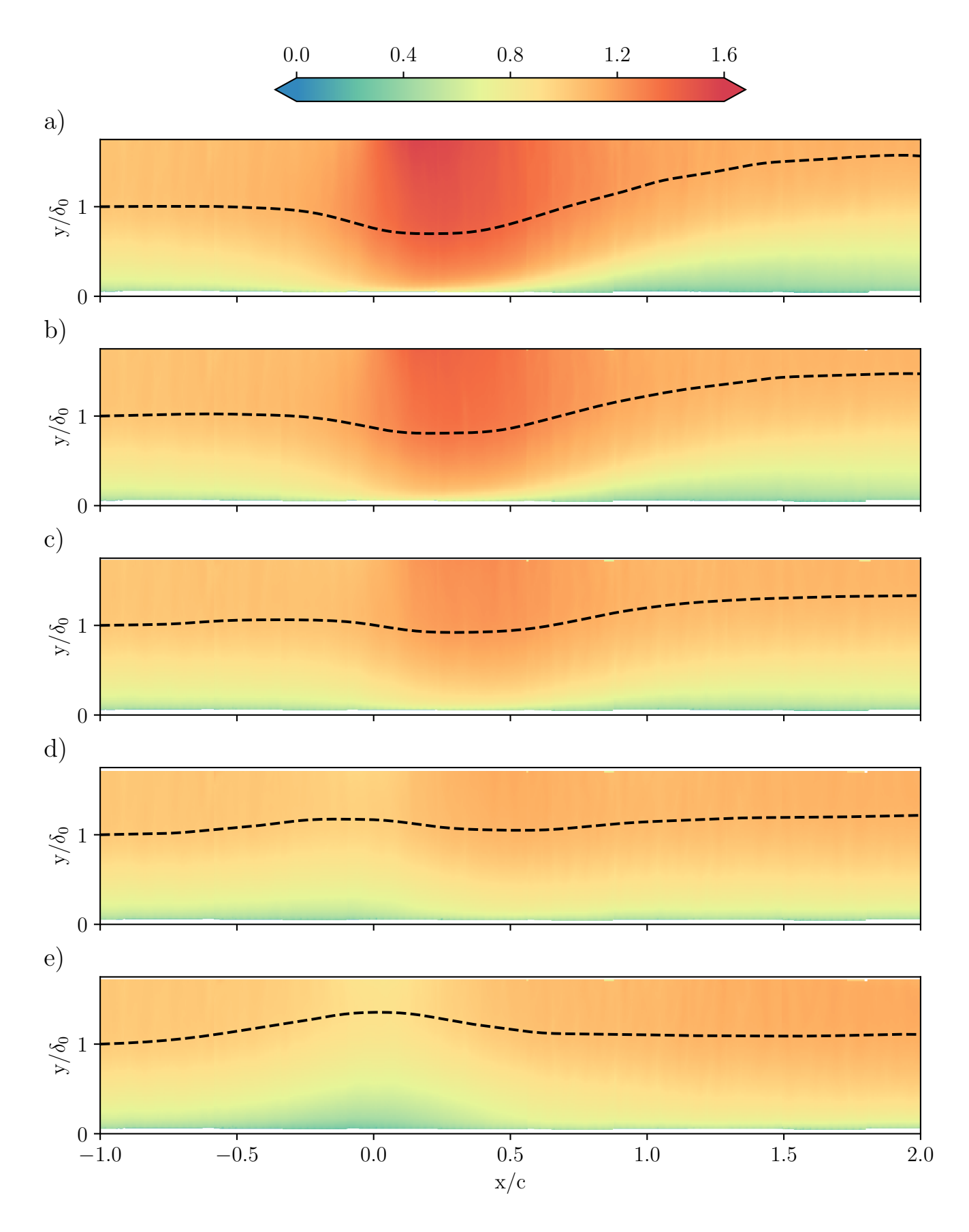


Figure 3: Velocity field plots of the mean streamwise velocity, U/U_{∞} , from x/c=-1 to 2. U_{∞} is the velocity from the pitot at x/c=-1. The black dashed line represents δ , marking the boundary layer edge, determined using the method described in Vinuesa et al. (2016). The five subfigures correspond to: (a) -8° , (b) 4° , (c) 0° , (d) 4° , and (e) 8° .

wall-normal direction due to the influence of the wing. Starting with the boundary layer thickness, as expected from past literature, the PG history has a clear effect. FPGs suppress the boundary layer, while APGs increase its thickness.

The leading cause of variation in the boundary layer thickness is the change in the outer region and, consequently, the wake strength. The friction velocity (U_{τ}) must first be estimated to examine the wake region. From previous work, it is assumed that the roughness length scale, y_0 , is invariant to pressure gradient history (Vishwanathan et al. (2023); Preskett et al. (2025)) and, for this surface, is taken to be 0.000462 m (Preskett et al. (2025)). Using this value along with equation 1, U_{τ} can be determined. The log-law limits for finding U_{τ} are defined as $0.02 < y/\delta < 0.2$, requiring at least 15 points for profile fitting where possible. In regions where this is not feasible due to significant boundary layer suppression from FPG, the minimum fit length is set to 80% of the available data, as strong FPGs extend the log-law region well into the region typically considered as the outer region. The author's previous work, Preskett et al. (2025), compared the fitting of the log-law region using this method to independent skin friction measurements and found errors to be around 5% for the rough wall cases. This error is in line with the uncertainty in U_{τ} from Monty et al. (2011), which is estimated for $\beta > 2$ of around 5%. This fitting process allows the Re_{τ} to be calculated. This experiment's range of Re_{τ} values is between 12900 and 18500.

The method chosen for calculating Π is to look at the maximum deviation from the log region as done in Volino and Schultz (2023), given by equation 3. The maximum deviation occurs at the boundary layer edge, $y = \delta$, where the velocity is $U_{99}^+ = U_{99}/U_{\tau}$. The reason for selecting this method over alternatives, such as fitting equation 1 in deficit form, is its independence from a specific wake shape function. This eliminates the dependence on the chosen function, $W(\eta)$, as in positions of strong PG, it is seen that the outer region does not follow classical wake functions. The maximum uncertainty in Π is taken to be ± 0.30 for a 95% confidence interval based on the 5% uncertainty in U_{τ} . This uncertainty range covers the difference in Π seen in the PIV data and the hot wire data with independent skin friction measurements of Preskett et al. (2025).

$$\Pi = \frac{\kappa}{2} \left(U_{99}^{+} - \frac{1}{\kappa} \ln \left(\frac{\delta - d}{y_0} \right) \right) \tag{3}$$

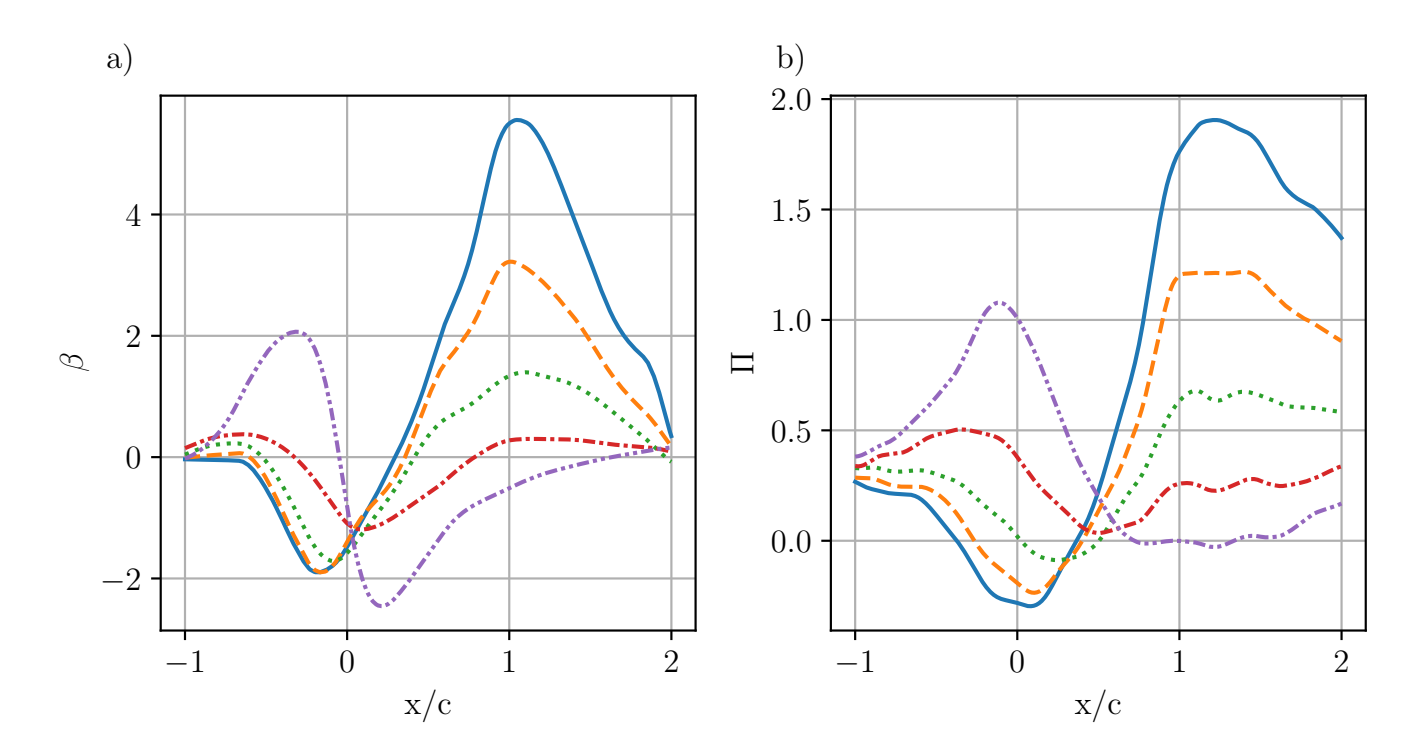


Figure 4: (a) Estimated variation in β using U_{τ} estimated from the velocity profile with δ^* measured from the velocity profile. (b) Variation in Π with the streamwise position for the five cases. Linestyles and colours are given in table 1.

The flow history can be represented by the parameter β as was seen in equation 2. An estimate of the β history is presented in figure 4a using U_{τ} obtained as explained above, along with the directly measured pressure gradient

and δ^* obtained from the PIV flow fields. To account for the lack of data in the near-wall region, a linear profile is assumed from the first data point to zero at the wall. At 9.03m, taking the HWA data results from Preskett et al. (2025) and replacing the near wall data with this method results in less than 3% error. A positive β value means an APG, while a negative value means an FPG. The highest β value seen is 5.6 for the -8° case at x/c = 1.0, while the lowest value is -2.5 at x/c = 0.2 for the 8° case. The β histories closely follow the shape given by the pressure gradient history. As with the PG history, there is a region in which all the cases cross over at $x/c \approx 0$. While for $dC_p/d(x/c)$, it occurs at $x/c \approx 0.25$.

This work examines the variation in flow structures, specifically focusing on the lag in the flow's response to these structures. Before analysing the structures and turbulent events within the flow, the lag observed in the mean flow for different PG histories is first examined. The turning points, these being the minimum and maximum points within the data, in the streamwise variation of the properties being compared, were analysed to achieve this. While cross-correlation was considered a method for determining lags, however, challenges were found due to the distribution only having two turning points. This was made worse by the shape of the distribution of some properties, which had significant plateaus. Consequently, the position of the peaks was chosen as a repeatable method, although this approach has the drawback of not being based on the shape of the distribution between the turning points.

	τ_1/δ_0	$ au_2/\delta_0$	$ au_{avg}/\delta_0$
-8°	-1.65	-1.41	-1.53
-4°	-1.95	-	-1.95
0°	-2.27	-	-2.27
4°	-2.09	-	-2.09
8°	-1.50	-	-1.50

Table 2: Location of the two turning points (τ_1 and τ_2) in the value of Π as well as the average of the two quantities for different pressure gradient histories

Table 2 gives the lag of the first and second turning points of the Π distribution compared to β . A negative lag indicates that the β distribution leads the Π distribution. As shown in figure 4, β and Π are correlated. Consequently, the positions of corresponding turning points of the same type in both distributions were compared. The distribution of Π is shown in figure 4b. In some cases, there is no clear peak in the second half of the domain; instead, a plateau is found. These plateaus for the -4° and 0° cases occur around the turning point in β . Similarly, a plateau in Π is also seen in the 4° and 8° , with the minimum Π occurring in the middle of the plateau for the 8° case. These plateaus pose challenges when considering the second peak. Therefore, only the first peak in these cases shall be considered. The first peak lag, τ_1 , shows no clear trend with the pressure gradient type. There is a clear trend with the magnitude of the corresponding β peak strength; a stronger PG leads to a faster flow response. The -8° and -4° cases have very similar β histories up to $x/c \approx 0.25$ as shown in figure 4a. These results in very similar Π distributions up to this point, with the lags being similar; however, a 20% difference is seen in the first peak lag due to the sensitivity of the method.

3.1 Integral Pressure Gradient History

The observed differences in the lags for the cases show a different method for predicting the wake strength. In the work of Preskett et al. (2025), it was seen that it is possible to predict the Π and, therefore, C_f based on the integral of the pressure gradient history and the local conditions at the measurement point. Defining $\Delta\beta$ as given in equation 4, Preskett et al. (2025) showed there to be a relationship based on single point measurements between $\Delta\Pi$ and $\Delta\beta$ where $\Delta\Pi = \Pi^{PG} - \Pi^{ZPG}$. This equation captures the upstream PG history in the integral of the PG history. It builds on the analysis of Vinuesa et al. (2017), which used the integral of β to predict skin friction. $\Delta\beta$, instead of requiring the complete β history, assumes that U_{τ} and δ^* retains some of the history of the upstream flow. Previous work has calculated $\Delta\beta$ based on all available pressure gradient history, which is often easier to obtain than the complete flow field measurements. This is from one chord upstream of the aerofoil to the measurement point, one chord downstream of the trailing edge.

$$\Delta \beta = \left(\frac{\delta^*}{\tau_w}\right)_{DS} \left[\frac{1}{x_{DS} - x_{US}} \int_{x_{US}}^{x_{DS}} \left(\frac{dP}{dx}\right) w(x) dx\right]$$
where $w(x) = \frac{x - x_{US}}{x_{DS} - x_{US}}$ (4)

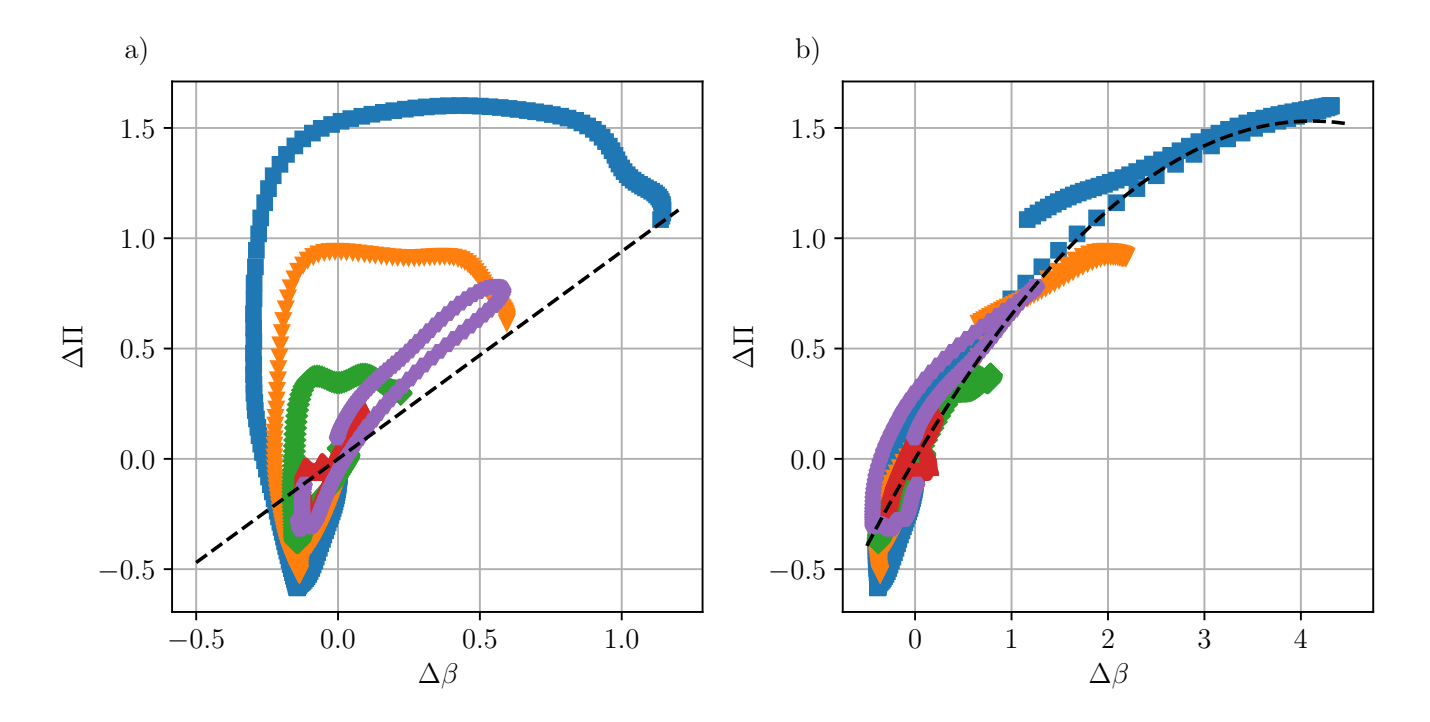


Figure 5: Variation of Π with $\Delta\beta$ for the five PG cases. (a) $\Delta\beta$ calculated using an integration length, L, of 3.75m and the black dash line showing the linear model given by Preskett et al. (2025). (b) $\Delta\beta$ calculated using L of 1.16m and the resulting best fit 2nd-order of all cases as given by equation 5.

This result can be examined using the PIV data by analysing the variation in $\Delta\beta$ versus Π . Figure 5a shows the variation of $\Delta\Pi$ with $\Delta\beta$ as defined by equation 4 with L=3c as in Preskett et al. (2025). The black dashed line in figure 5a shows the prediction of $\Pi=0.94\Delta\beta$ from Preskett et al. (2025). The PIV data does not show the trends seen in Preskett et al. (2025). This is because the model in Preskett et al. (2025) was based upon the data at x/c=2, where it can be seen in the PIV data that there is good agreement with the predicted model. The distribution of $\Delta\beta$ is defined by two variables: the weighting function w(x) and the integration length, $L=x_{DS}-x_{US}$. The integration length is particularly critical, as it determines how much of the upstream pressure gradient history is considered. Previous work of Bobke et al. (2017) has suggested at least 7δ of similar β history is required for profiles to recover to the same state, though this was seen in mild PG regions.

The variation in Π through the domain can be used to estimate the extent of upstream PG history required to capture flow effects. A linear weighting function, with values of 0 and 1 at the upstream and downstream references, will be used, as per previous work. Firstly, the optimum value of the integration length, L, shall be calculated for each case individually before considering all cases together and obtaining a single value of L. The optimum value of L shall be based on the mean error between $\Delta\Pi$ and $f(\Delta\beta)$. In our previous work, we hypothesised that the pressure gradient history further upstream is less important than the information just immediately upstream. It has been seen that a linear relationship between $\Delta\beta$ and $\Delta\Pi$ fails to capture the trends in regions of strong local PG acceptably. This suggests that the relationship is perhaps stronger than a simpler linear one. To capture this, a second-order curve given by $A\Delta\beta^2 + B\Delta\beta$, is used. This is not the only method possible to capture the non-linearity seen in the data. Other methods, such as changing the weighting function (for example, using the error function), would also allow the non-linearity to be captured, changing the contribution of the $\Delta\beta^2$ term. In this work, the second-order term is chosen rather than modifying the weighting function, as a linear weighting form reduces the risk of over-fitting and is more robust given the limited data available. Furthermore, as noted by Monty et al. (2011), the relationship between Π and β is strictly an increasing function. With a simple and constant integration length throughout the domain, only the pressure gradient data upstream of the region of interest is required.

Table 3 shows the optimum integration length for each of the five cases. It shows that FPG to APG cases (-8° , -4° and 0°) require shorter integration lengths than APG to FPG cases (4° and 8°). While there is variation in the optimum value of L, having a single value of L for all cases would be more useful. The process will be the same as outlined previously. The fitting of $f(\Delta\beta)$ is done using all five cases together and the error of all cases combined. The optimised value of L is 1.17m or 0.94c, equating to 6.7 δ_0 ; significantly less than the value of 3c used

Table 3: Variation in optimum integration length, L for $\Delta\beta$ calculated by comparing the error between the normalised $\Delta\beta$ and Π distributions.

in Preskett et al. (2025). Using a Monte Carlo simulation, the uncertainty in L is estimated to be 0.036 m, which is small compared to the value of L. This small uncertainty is due to the large amount of data upon which the model is based, making small variations have little effect. The $\Delta\beta$ distribution and corresponding $\Delta\Pi$ values are shown in figure 5b. Also shown is the corresponding best-fit 2nd-order curve as given by equation 5.

$$\Delta\Pi = -0.090\Delta\beta^2 + 0.744\Delta\beta \tag{5}$$

The agreement between the PIV data and equation 5 in figure 5b is seen to be reasonable. The agreement at higher $\Delta\beta$ is better than that at lower values of $\Delta\beta$ where more scatter is seen. The chosen 2nd-order curve best fits the overall shape of the data and supports the decision to use a 2nd-order curve. This result supports the conclusion of Preskett et al. (2025) that it is possible to predict the variation in Π using $\Delta\beta$. It is noted at this point that the derived curve is specific to the dataset. Therefore, it is not known at this time whether this will transfer to other datasets due to a lack of high Reynolds number rough wall data with different PG histories in past literature. Going forward in this work, when calculating $\Delta\beta$, the value of L will be 0.94c (1.17 m). At this stage, it is unclear if equation 5 can be universally applied across all PG flows.

4 Turbulence and Structures

This section will examine the mean $\overline{u}\overline{u}$ and $\overline{u}\overline{v}$ profiles and how they vary at different stations through the PG history. The relative contribution of different flow events (sweeps and ejections) to the overall Reynolds shear stress is examined for different PG histories. The final part of this section will look at structures within flow using two-point correlation. The effect of PG on structures' length, height and inclination will also be discussed.

4.1 Turbulence Profiles

Previous works, such as Bobke et al. (2017), have studied Reynolds stresses due to the retention of PG effects. In this analysis, we shall use the value of L_{avg} as in figure 5b to compare profiles at similar conditions. The non-linearity of equation 5 indicates that the response of the flow structures differs with PG strength. This is especially true for the large-scale structures which dominate the wake region (Monty et al. (2011)). Since these structures in the outer region vary with wake strength, we now consider whether $\Delta\beta$ can be used to predict the turbulence within the flow. First $\overline{u}\overline{u}^+$ at $\Delta\beta$ of -0.35 is presented in figure 6a. Two distinct groups of cases are seen despite having matched $\Delta\beta$ group by the different transparencies. Looking first at the group of three, the -8° , -4° and 0° cases are taken at x/c = -0.12, -0.07 and -0.03. The group of two shown with lower transparency (resulting in a fainter line) is taken at $x/c = \approx 0.47$ for the -8° and -4° cases. There is some small variation in the position of the curves relative to each other, this being due to the uncertainty of the fitting of U_{τ} . The uncertainty in U_{τ} along with the uncertainty due to the PIV results in an uncertainty of around 20% in $\overline{u}\overline{u}^+$ and $\overline{u}\overline{v}^+$. Therefore, this should be taken into consideration when comparing the different profiles. Therefore, the shape will be more important for close curves when examining the effects of PG history. While all five curves in figure 6a have the same $\Delta\beta$ value, they do not have the same local β value. The group of three are experiencing an FPG with $-1.85 < \beta < -1.65$ while the group of two is an APG with $\beta = 1.11$ and 0.72 for the -8° and -4° cases. Therefore, it is important to consider the history and local conditions when comparing cases.

The $\overline{u}\overline{u}^+$ profiles show that an FPG suppresses the turbulence while an APG increases the turbulence. As the PG switches, the initial changes in the turbulence are seen closer to the wall; the outer region takes longer to respond. This is because energised structures in the outer region take longer to respond. These trends are seen in both $\overline{u}\overline{u}^+$ and $-\overline{u}\overline{v}^+$ in figure 6b. Between the two groups, there is a collapse in the outer region since the PG sign change occurs just upstream of the measurement station for the two cases at x/c = 0.45.

Extending this analysis further, conditions with matched $\Delta\beta$ and β_{local} can also be found. In figures 6c and d profiles are taken at $x/c=1.95,\,1.77$ and -0.11 for the -8° , -4° and 8° cases. For these three cases, $\Delta\beta\approx1.2\pm0.11$ and $\beta\approx0.9\pm0.06$. For the previous cases, one group had experienced one PG type, and the other group had just started experiencing the second at the measurement stations. In current cases, the -8° and -4° , have experienced

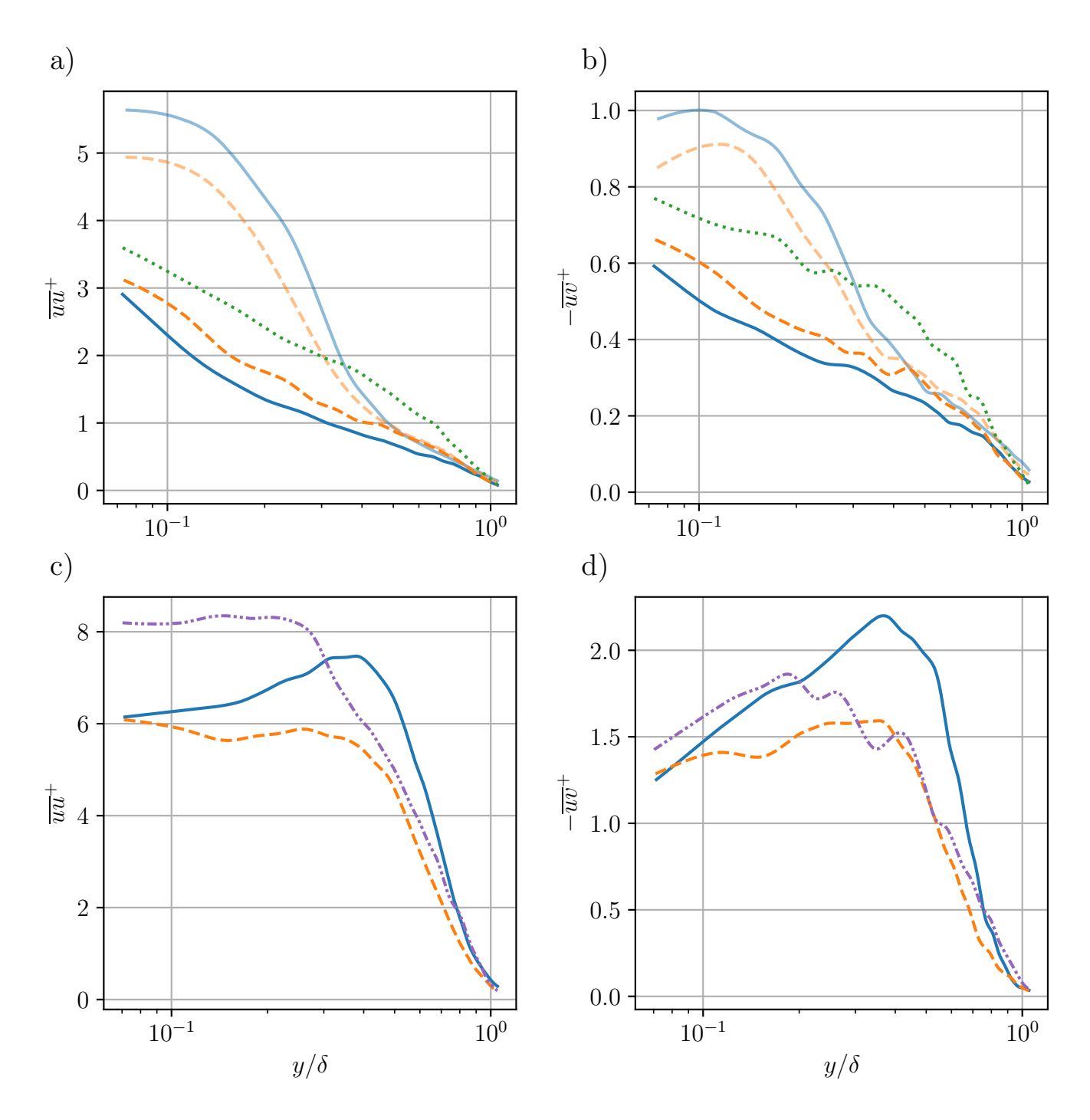


Figure 6: Mean turbulence profiles for (a) Shows profiles of \overline{uu}^+ , where $\overline{uu}^+ = \overline{uu}/U_\tau^2$. The group of three shown with no transparency are the -8° , -4° and 0° cases are taken at x/c = -0.12, -0.07 and -0.03. The group of two with higher transparency, resulting in a fainter line to distinguish the groups, show the -8° and -4° at x/c = 0.47 and 0.46. (b) Shows profiles of $-\overline{uv}^+$, where $\overline{uv}^+ = \overline{uv}/U_\tau^2$ for the cases shown in a. (c) Shows profiles of \overline{uu}^+ for the -8° , -4° and 8° cases at x/c = 1.95, 1.77 and -0.11. (d) Shows $-\overline{uv}^+$ profiles for the cases given in c. Colours and line styles are given in table 1

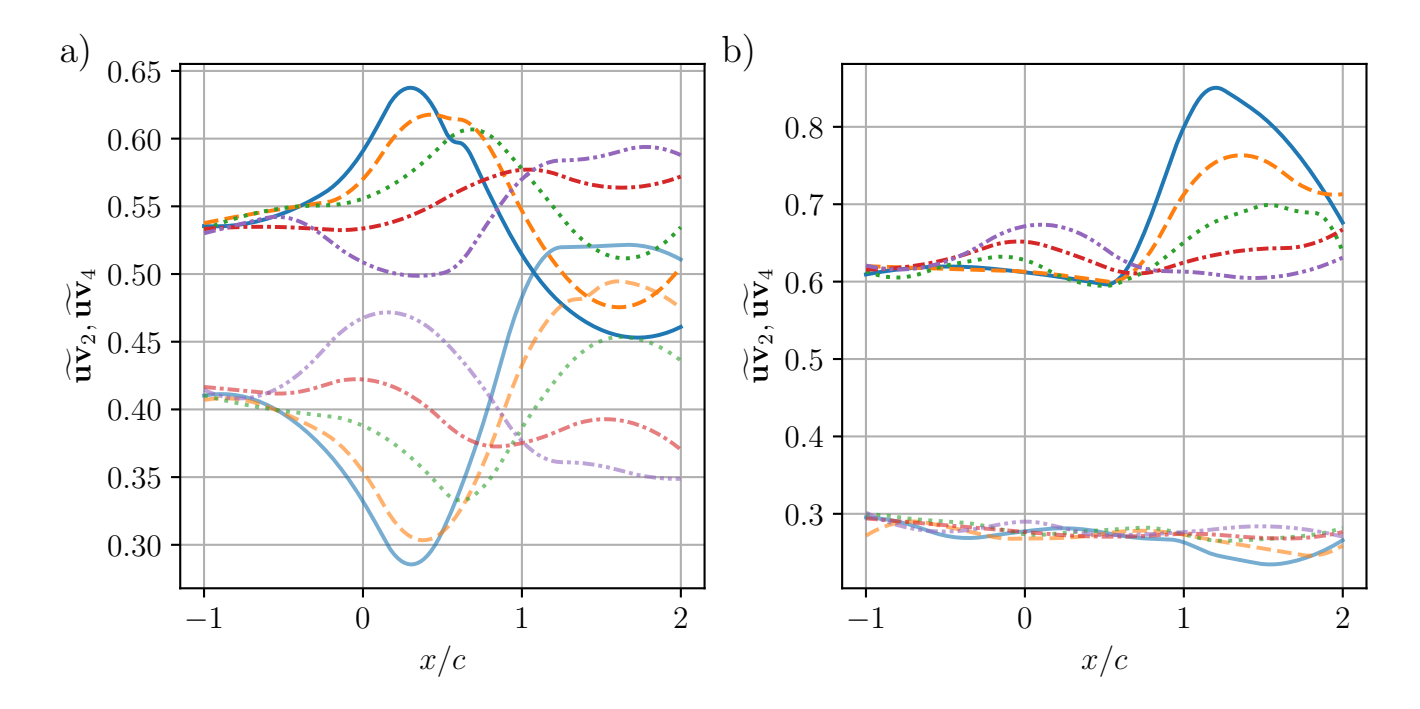


Figure 7: Variation in \widetilde{uv}_2 and \widetilde{uv}_4 with streamwise position for the five cases. \widetilde{uv}_4 is distinguished from \widetilde{uv}_2 by its higher transparency, and in both sub-figures is the lower set of curves. The two sub figures show different y_{ref}/δ values (a) 0.2 and (b) 0.6. Colours and line styles as set out in table 1.

both FPG and APG, along with the 8° case, which has only experienced an FPG. The profile shapes clearly differ despite having very similar $\Delta\beta$ values and the same local β . As seen in previous works such as Monty et al. (2011), there is a clear peak in the outer region of the -8° case and a smaller one in the -4° cases. This is caused by the strong APG energising the outer region structures. In figure 6a and b, there was some collapse seen in the outer region, in 6c and d, this collapse is only seen after $y=0.8\delta$. There is a slightly better collapse for $\overline{u}\overline{u}^+$ and $\overline{u}\overline{v}^+$ for the -4° and 8° cases from $y=0.6\delta$. The lack of collapse shows that history is retained much longer in the turbulence structures compared to the mean flow for which L_{avq} was calculated.

4.2 Sweep and ejection events

Sweep and ejection events, also known as Q4 and Q2 events, dominate flow structures responsible for transporting turbulence to and from the wall. The method outlined by Lu and Willmarth (1973) will be employed to perform quadrant analysis and examine their contribution. This method introduces a 'hole' into the quadrant analysis; anything outside the hole significantly contributes to the overall \overline{uv} . Any fluctuation inside the hole is a small fluctuation present with little contribution to the overall \overline{uv} . The hole boundaries are given by |uv| = Hu'v' where u' and v' are the local rms at a given location within the flow. The hole size will affect the number of events included in this analysis; H was set as 1, as in Gul and Ganapathisubramani (2021).

Figure 7 shows how the relative contribution of Q2 and Q4 events to the overall \overline{uv} changes with the streamwise position at different y/δ . The contribution ratio, \widetilde{uv}_i , is calculated as defined by Lu and Willmarth (1973). Overall, it is seen that moving away from the wall, \widetilde{uv}_2 increases while \widetilde{uv}_4 reduces. This aligns with previous results for a rough wall boundary layer; the same trends are seen in Gul and Ganapathisubramani (2021). Looking firstly at figure 7a for $y=0.2\delta$, on the edge of the log layer, we see an obvious inverse relationship between \widetilde{uv}_2 and \widetilde{uv}_4 . It is seen that FPG increases \widetilde{uv}_2 while at the same time reducing \widetilde{uv}_4 . APGs have the opposite effect, reducing \widetilde{uv}_2 while increasing \widetilde{uv}_4 . For the majority of the domain, \widetilde{uv}_4 is less than \widetilde{uv}_2 however, for strong APGs \widetilde{uv}_4 is larger than \widetilde{uv}_2 . This is seen in the -8° case between x/c=1.1 and x/c=2. The lags in both \widetilde{uv}_2 and \widetilde{uv}_4 are very similar, with the turning points of both variables occurring at similar positions.

Deep into the outer region for $y/\delta = 0.6$, a very different trend is shown in figure 7b. \widetilde{uv}_4 contribution is seen to be less than 30% compared to more than 40% at $y/\delta = 0.2$. The variation in \widetilde{uv}_4 through the domain is also small compared to heights nearer the wall. The PG history has no clear trend with the \widetilde{uv}_4 distribution. For $y/\delta = 0.6$, the max variation from the mean value is less than 5%. This small derivation comes in the -8° case, which has the

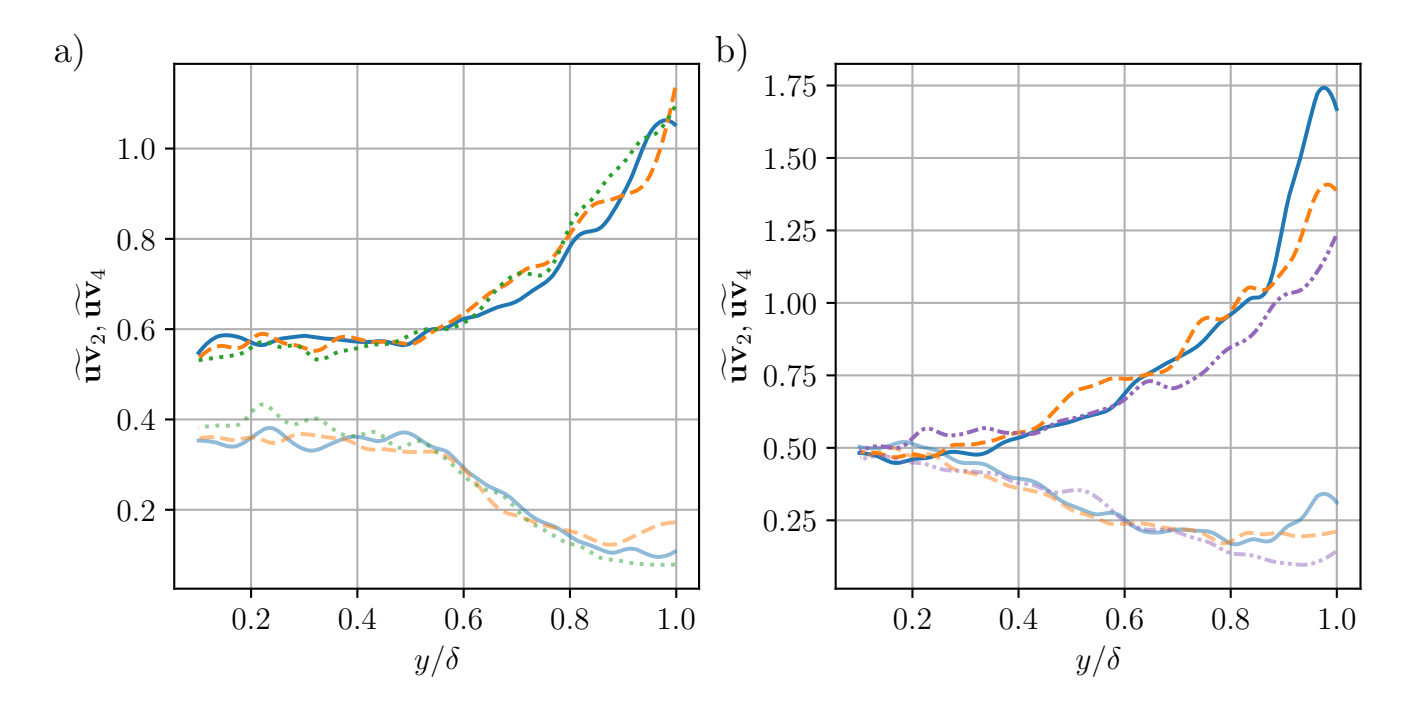


Figure 8: Variation in \widetilde{uv}_2 and \widetilde{uv}_4 with wall normal position, y. \widetilde{uv}_4 is distinguished from \widetilde{uv}_2 by its higher transparency, and in both sub-figures is the lower set of curves. (a) Shows the -8° , -4° and 0° cases are taken at x/c = -0.12, -0.07 and -0.03. (b) Shows profiles for the -8° , -4° and 8° cases at x/c = 1.95, 1.77 and -0.11. Colours and line styles as set out in table 1.

strongest APG, with a small decrease in \widetilde{uv}_4 . There is an inverse relationship for \widetilde{uv}_2 compared to $y/\delta = 0.2$ at these two heights. At $y/\delta = 0.6$, there is only a small effect in the FPG region of the -8° , -4° and 0° cases. There is a clear flow reaction to the APG region for these cases, with an increase in \widetilde{uv}_2 opposite to what was seen at $y/\delta = 0.2$.

Figure 8 looks at the variation in \widetilde{uv}_2 and \widetilde{uv}_4 through the boundary layer for the conditions seen in figure 6. Starting with figure 8a presents the cases shown in 6b for the -8° , -4° and 0° cases at x/c=-0.12, -0.07 and -0.03. This group of three cases are chosen since the turbulence profiles in figure 6b profiles show good collapse with the same value of $\Delta\beta$. The -8° and -4° cases have experienced both an FPG followed by an APG, while the 8° cases only have an APG. The first observation is that the contribution of \widetilde{uv}_2 and \widetilde{uv}_4 is constant up to $y=0.6\delta$ around 0.56 and 0.36, respectively. After $y=0.5\delta$, \widetilde{uv}_2 increases, with the rate of change increasing as the position in the boundary layer moves further from the wall. \widetilde{uv}_4 decreases away from the wall linearly from 0.5δ to 0.8δ before the contribution levels off around 0.1. All the cases presented here exhibit good collapse despite the varying values of β , indicating a stronger dependence on the local PG type rather than its magnitude. This outcome is expected, as the \overline{uv}^+ profiles for these cases have similar shapes across the different cases.

Figure 8b shows \widetilde{uv}_2 and \widetilde{uv}_4 for the -8° , -4° and 8° cases at x/c=1.95, 1.77 and -0.11. These cases are explored since in figure 6d showed differences in the \overline{uv}^+ despite having the same $\Delta\beta$ and β at the measurement location. The positions chosen have experienced different upstream histories, with two cases having experienced FPG and APG, while the other only an APG. Examination of the contribution of sweeps and ejection will allow differences to be explored. Some differences exist from those experiencing an FPG in figure 8a. Firstly, the \widetilde{uv}_2 and \widetilde{uv}_4 are similar near the wall around 0.5 constant up to around 0.3δ compared to the 0.5δ for the FPG measurement stations. The collapse between cases is not as good as was seen in figure 8a; however, the overall trends are the same. These differences are expected since the profiles of \overline{uv}^+ show clear differences due to the retained PG history. However, the differences in shape seen in figure 6d around 0.4δ are not seen in the profiles of \widetilde{uv}_2 and \widetilde{uv}_4 .

4.3 Flow Structures

The analysis above highlights how various parts of the boundary layer respond differently to varying PGs. This section will consider the spatial structures and how they vary in size and inclination through the domain. To do this, we shall use two-point spatial correlation to understand these variations and see how their shape changes. Two-point spatial correlation is carried out using equation 6 (Gul and Ganapathisubramani (2021)) on the fluctuations of the

velocity fields captured from PIV. The correlation coefficients will vary between -1 and 1 throughout the domain, with the reference point being the only point with a value of 1.

$$R_{u_1 u_2} = \frac{\overline{u_1(x_{ref}, y_{ref})u_2(x_{ref} + \Delta x, y_{ref} + \Delta y)}}{\sqrt{u_1^2(x_{ref}, y_{ref})u_2^2(x_{ref} + \Delta x, y_{ref} + \Delta y)}}$$
(6)

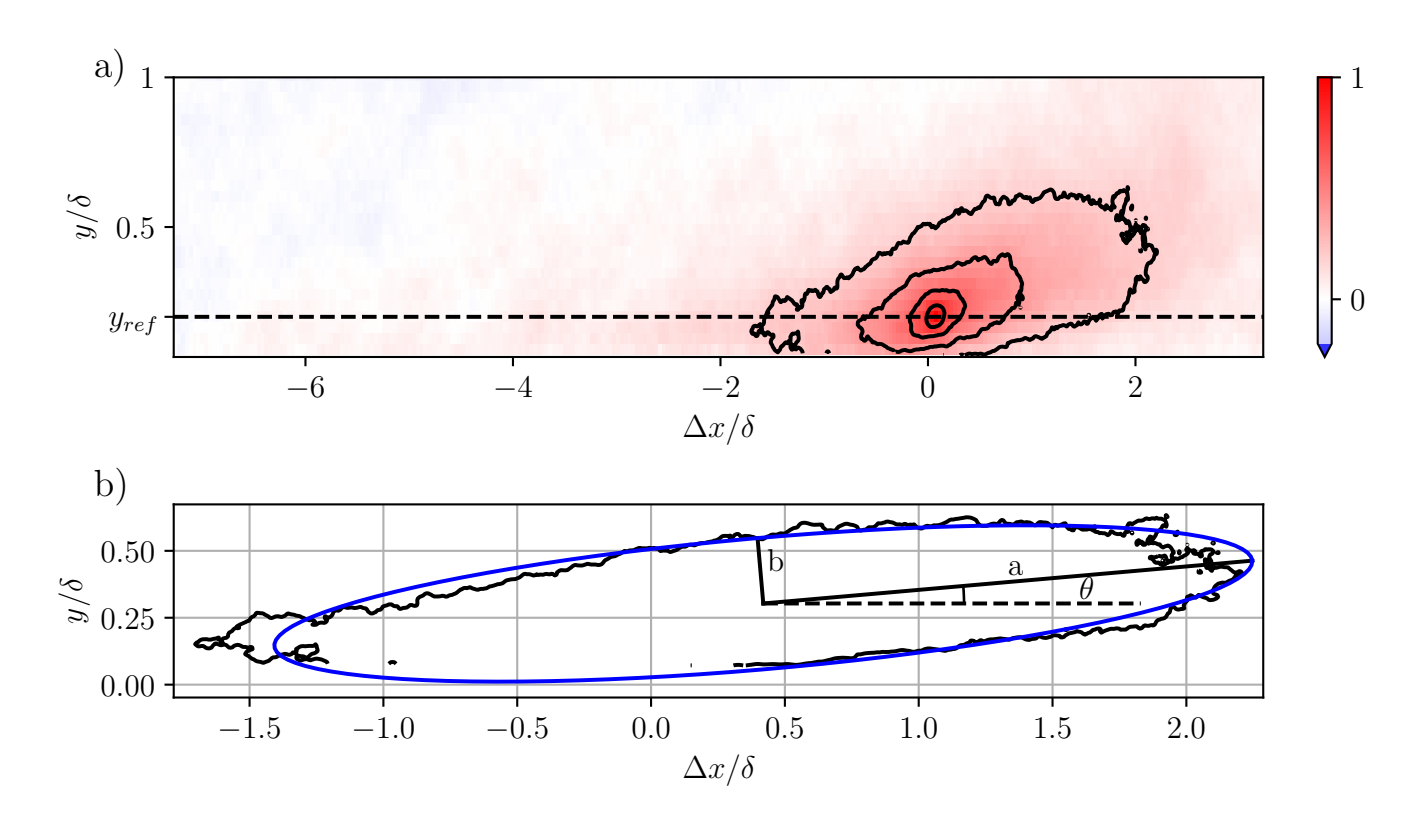


Figure 9: a) Example R_{uu} field for -8° case with the reference point taken as x/c=0.25 and $y/\delta=0.2$. Contours of correlation levels corresponding to 0.2, 0.4, 0.6 and 0.8 are plotted. b) Largest contour at 0.2 level with the blue ellipse showing the ellipse resulting from fitting the contour from which a, b and θ can be extracted corresponding to the dimensions shown.

Figure 9a shows a typical correlation field for R_{uu} . For this example, x_{ref} is taken to be x/c = 0.25 and $y_ref = 0.2\delta$ where δ is the local delta at the reference point. Shown are four contour levels, the largest contour being the lowest correlation value of 0.2 and the smallest 0.8. The lower correlation contours can be interpreted as representing the large streamwise structures within the flow, while the higher correlation values correspond to smaller scales. At a contour level of 0.2, the structure extends over 2δ downstream and 1.5δ upstream. This structure extends from the wall up to 0.6δ , showing correlated structures influencing all boundary layer regions. The following analysis will use contour levels of 0.2 and 0.6. These have been chosen since 0.2 is the largest level where the contour shape can be said to be given by an ellipse. Below this level, the wall truncates too much of the contour, meaning an ellipse cannot describe its shape reliably. A level of 0.6 is chosen since the contours above this level are small and close circular in shape, and thus, their major and minor axis are very close in size.

The correlation fields obtained enable the examination of the structures; however, a method is needed to quantify their size and shape. This is achieved by fitting an ellipse, as shown in figure 9b. The ellipse can be defined using equations 7 and 8. The centre is defined at (x_0, y_0) with a major axis (a), minor axis (b) and angle of inclination (θ) . Figure 9 shows the largest contour for a level of 0.2 as extracted from figure 9a given by the black line. The blue ellipse shows the result of the fitting process using equations 7 and 8. As can be seen, the ellipse provides a suitable representation of the shape of the contour for R_{uu} . The major and minor axes may switch positions for nearly circular contours such that the major axis is predominantly oriented in the wall-normal direction. This will lead to jumps in the values of a and b; hence, care must be taken when interpreting the smaller contours.

$$x = x_0 + a\cos(t)\cos(\theta) - b\sin(t)\sin(\theta)$$

$$y = y_0 + a\cos(t)\sin(\theta) + b\sin(t)\cos(\theta)$$

$$\text{where } t \in [0, 2\pi]$$
(7)
(8)

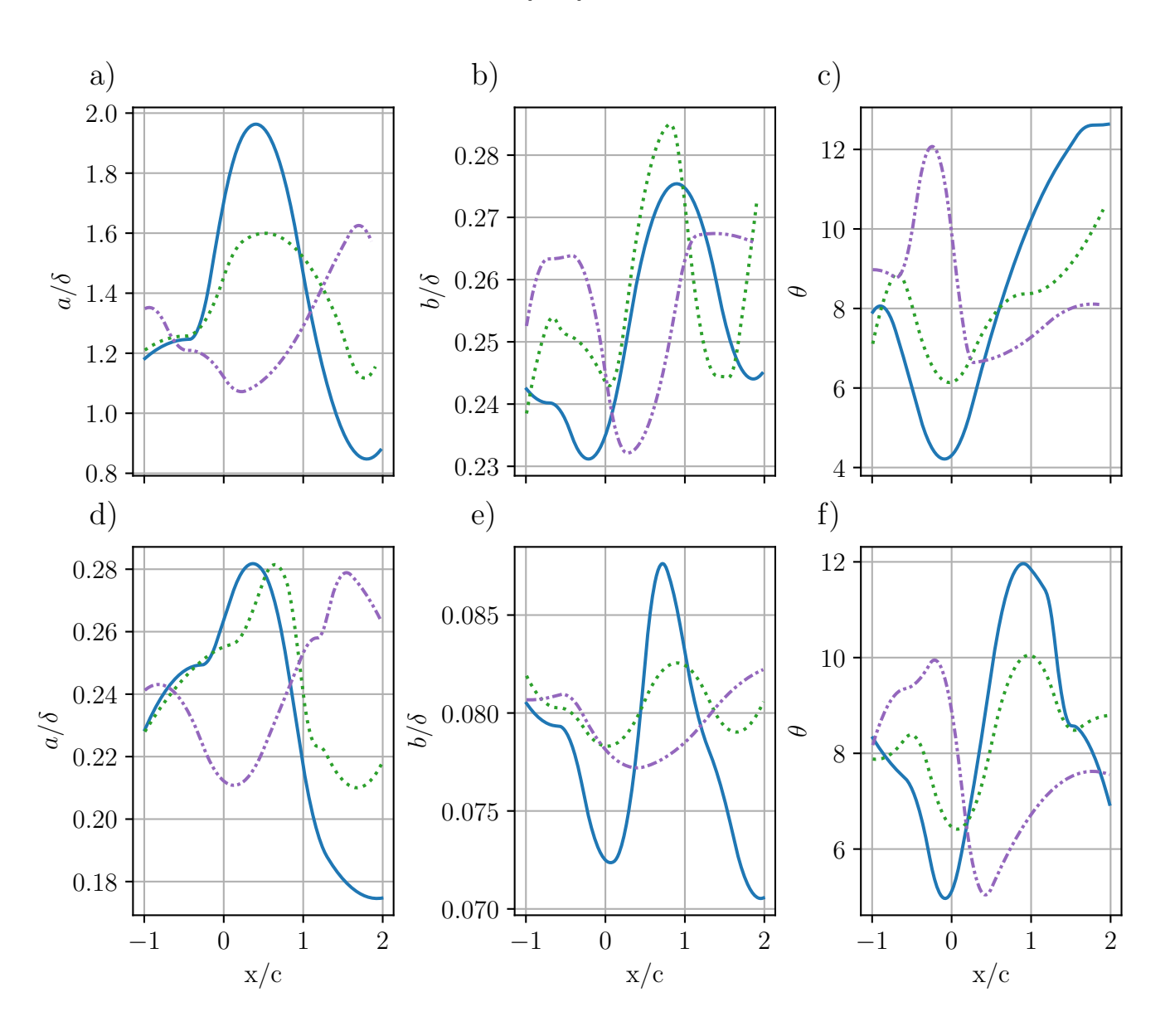


Figure 10: Variation of flow structure properties resulting from contour fitting with $y_{ref} = 0.2\delta$. (a-c) shows variation in a/δ , b/δ and θ , respectively, for a contour level of 0.2, representative of the large scales within the flow. (d-f) Shows the variation in a/δ , b/δ and θ , respectively, for a contour level of 0.6, representative of the small scales within the flow. Only the -8° , 0° and 8° cases are shown with colours and linestyles in table 1.

Using this method, it is now possible to examine the variation in flow structures through the different pressure gradient histories. The first part of this analysis will look at the variation in properties at the edge of the log layer (0.2δ) for both large and small structures. Figures 10a-c shows the change in variables for the large-scale structures at a contour level of 0.2, while figures 10d-f the small scales at a level of 0.6. For clarity in the presentation of figures, only the cases of -8° , 0° , and 8° are included. However, the other cases follow similar trends to the ones shown. Ellipses are only fitted where the complete contour is available in the field of view. This results in gaps in the domain where fitting cannot be completed near the edges of each field of view. For large-scale structures, the gaps in the domain increase compared to those for the small scales since the large scales take up more of the domain. The curves

shown in figure 10 use univariate splines with a maximum of five turning points to estimate the distribution. When normalising the length scale and choosing the reference location, the local δ is used. To estimate the uncertainty in the fitting, we shall use the mean deviation from the average trend lines. For the length scales of both the small and large scales, the mean deviation is less than 6% from the trend lines shown in figure 10. The variation in the inclination is higher, with a maximum variation of 12% seen for the large-scale structures.

The first variable to consider is the major axis representing the streamwise length of the structures within the flow shown in figures 10a and d. The large-scale structures range from 1.6δ to 4δ since a is only half the structure size. However, the small-scale structures from 0.36δ to 0.56δ are up to eight times smaller than the large-scale structures. The overall trend shown by the major axis is that FPGs increase the streamwise length of the structures, whereas APGs reduce it for both small and large scales. Both levels have curves starting at approximately the same value, one chord upstream of the aerofoil, considering experimental noise. This is expected, as the flow is assumed to be zero pressure gradient (ZPG) up to this point, meaning all cases share the same flow history. This can also be seen in the Reynolds stress and value of Π , which are all similar at this point. However, beyond this point, the varying flow histories lead to significantly different values at x/c=2 due to the accumulated pressure gradient history. The small scale's major axis shows less dependence on the strength of the pressure gradient and more on the type. The -8° and 0° cases have very similar distributions of length scales despite the 0° case having a weaker pressure gradient. The weaker pressure gradient results in a delayed peak due to the weaker pressure gradient compared to the -8° case.

The variation seen in the minor axis is much less compared to the major axis. Taking the large-scale -8° case, the major axis sees changes of 65%, whereas the minor axis is only 14% from its initial value. Both the minor axis (figures 10b and e) and the inclination (figures 10b and e) shall be considered together. As is expected, an FPG suppresses the structures to be more parallel to the wall with a reduced wall of normal height, represented here with the minor axis. An APG has the opposite effect, 'pulling' the flow upwards, extending the minor axis and increasing the structure's inclination. The large-scale structures' inclination retains history for much longer than the streamwise or wall-normal length. This is based upon the inclination not reaching a turning point, unlike the major or minor axis, which both reach clear turning points in the second half of the domain. This is not seen in the small-scale structures where the inclination recovers to approximately its value before experiencing the PG history.

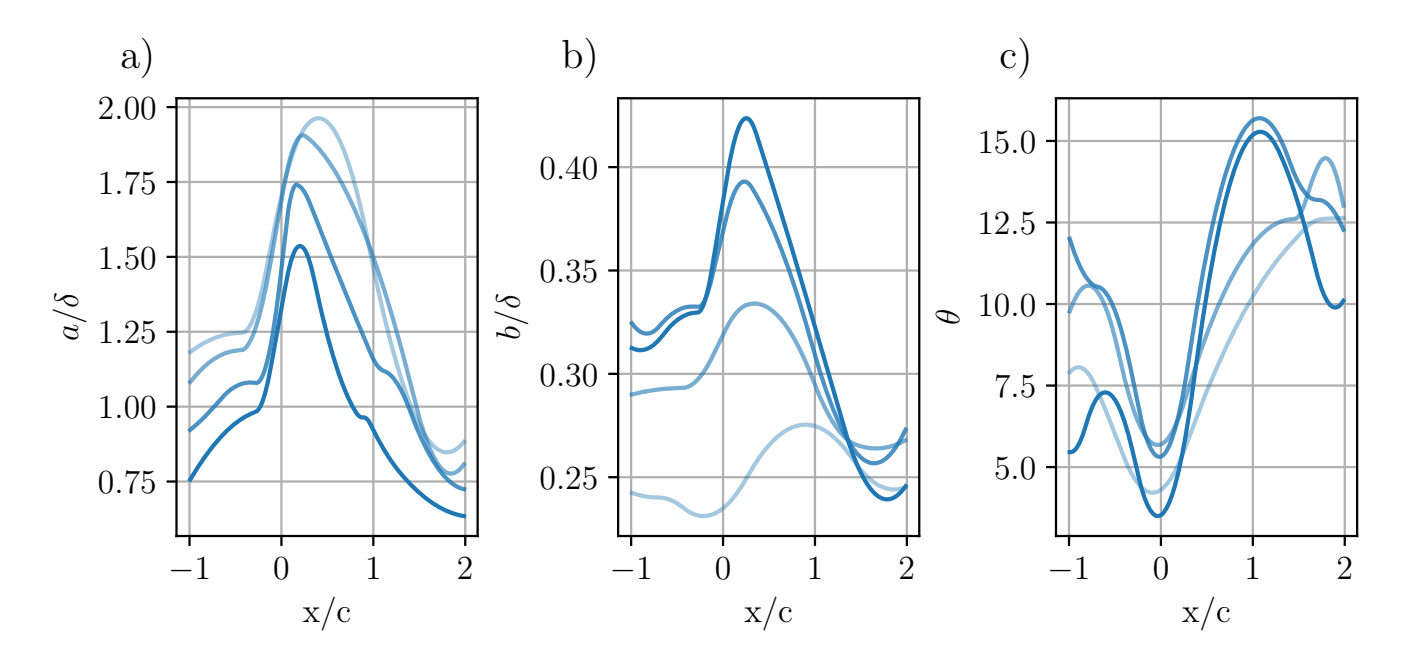


Figure 11: Variation in flow structures properties for the -8° case with varying y_{ref}/δ through the flow domain. The highest transparency case is for $y_{ref}/\delta = 0.2$, and the transparency is reduced up to $y_{ref}/\delta = 0.8$. (a) Shows variation in the major axis, $a\delta$. (b) Shows variation in the minor axis, $b\delta$. (c) Shows variation in the inclination, θ .

The preceding analysis has considered the variation in properties on the edge of the log layer. The final part of this work shall look at how different parts of the boundary layers respond. For this analysis, only the large-scale structures shall be considered since these are the most energetic structures within the flow. Looking at figure 11 a, the major axis decreases in size the higher up the boundary layer the reference point is taken. It can also be seen

that the closer to the wall the reference point is taken, the higher the lag the flow experiences. Briefly examining the lag of the first peak of a/δ with respect to β as was done for Π . For 0.2δ the lag with respect to β is $4.51\delta_0$ while for 0.8δ the value is $2.56\delta_0$. These values are larger than that τ_1 value seen when looking at the distribution of Π of ≈ 1.65 . Therefore, while the wake strength reaches its minimum, the flow structures still haven't reached their maximum streamwise length in the streamwise direction due to the FPG.

The minor axis, shown in figure 11b, becomes smaller the closer to the wall the reference point is taken to be. At 0.2δ , the trends are explained in the previous analysis, with the FPG suppressing the minor axis and the APG increasing it. However, for the outer points within the boundary layer, no response is seen to the FPG initially seen for the -8° case. This suggests that the outer part of the flow with the energetic large structures is unaffected by the FPG since they are further out from the wall and sense the incoming APG earlier than points near the wall. The inclination trends show no such trend; the response to the PG history at all y/δ values is similar. The two length scales show a clear trend with the starting position in the ZPG region around x/c = -1. For θ , however, there is no such clear trend with y_{ref}/δ . It can be seen, however, that structures in the outer layer reach a clear peak in the second half of the domain. Meanwhile, those near the wall do not reach a clear peak and slowly trend towards a plateau.

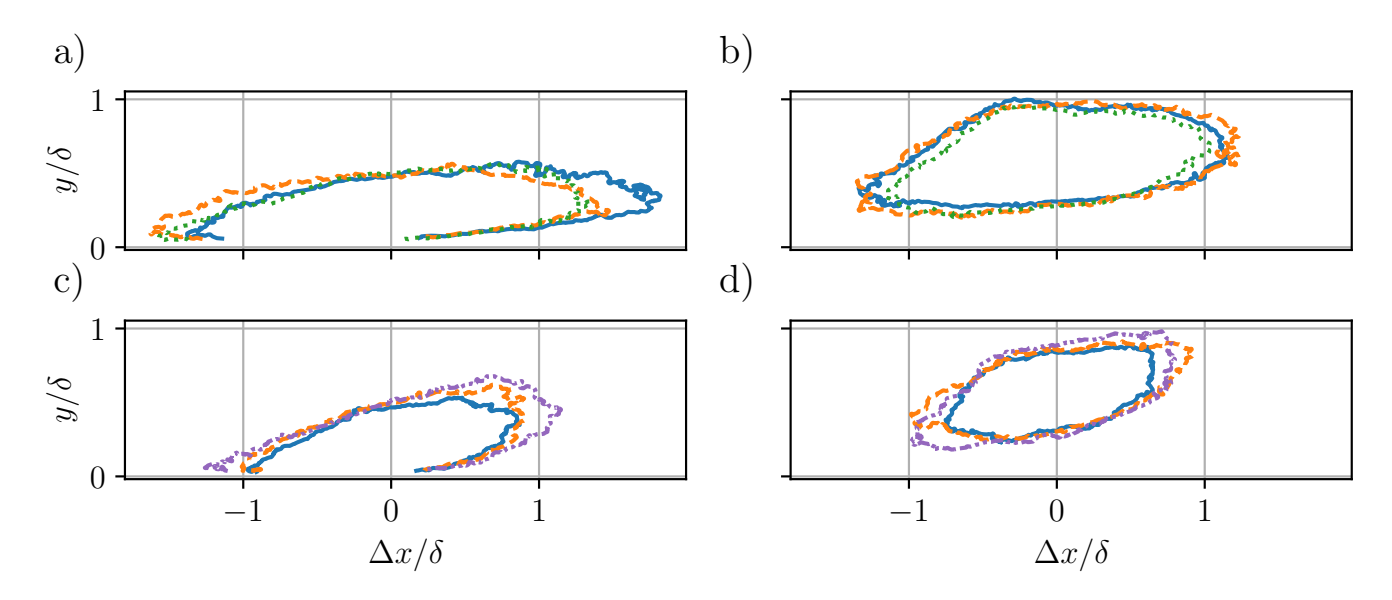


Figure 12: (a) Contours of $R_{uu}=0.2$ with $y_{ref}=0.2\delta$ for the -8° , -4° and 0° cases at x/c=-0.12, -0.07 and -0.03. (b) Contours of $R_{uu}=0.2$ with $y_{ref}=0.6\delta$ for the same cases in a (c) Contours of $R_{uu}=0.2$ with $y_{ref}=0.2\delta$ for the -8° , -4° and 8° cases at x/c=1.95, 1.77 and -0.11. (d) Contours of $R_{uu}=0.2$ with $y_{ref}=0.6\delta$ for the same cases in c. Colours and line styles are given in table 1

In previous sections, we have considered properties under matched conditions. The final property to consider at matched conditions is the large-scale structures present within the flow. Firstly the -8° , -4° and 0° cases at x/c=-0.12, -0.07 and -0.03 are considered which have matched $\Delta\beta$. Contours of R_{uu} at level of 0.2 with $y_{ref}=0.2\delta$ are shown in figure 12a. The inclination for the -8° and -4° cases is found to be $\approx 4^{\circ}$. The major axis length for these two cases is also similar with $a/\delta\approx 1.5$. The 0° case has a slightly lower major axis with $a/\delta\approx 1.4$ with an inclination of 6.2°. These values will be slightly different to the values that would be found from the curves in figure 10 since these curves are averaged from all data. Similar trends are seen in the outer region at $y_{ref}=0.6\delta$ in figure 12b where adelta is between 1.18 and 1.26. The inclination of the contours varies between 5.6° and 7.9°. These are consistently higher than those seen closer to the wall due to the inclination in the outer region responding before the near wall region. The collapse in the contours is to be expected since the turbulent profiles in figure 6a were seen to collapse for these cases.

The contours in 12c taken a $y_{ref}=0.2\delta$ for the -8° , -4° and 8° cases at x/c=1.95, 1.77 and -0.11. Here, there is much greater variation in the contour shapes despite both matching $\Delta\beta$ and β at the location of interest. The -8° and -4° cases have both experienced an FPG then APG, while the 8° case only an APG. There is some clear PG in the contour shapes. The 8° case has the largest a/δ at 1.28 while the -8° and -4° cases have a/δ of 0.86 and 0.98, respectively. The inclination of these structures increases from 11.6° to 15.1° as the angle of attack increases. In figure 12d where the cases are taken with $y_{ref}=0.6\delta$. Further away from the wall, the a/δ is much closer for all

cases between 0.72 and 0.89. The varying response time of different regions of the flow makes predicting properties difficult. The results presented in this section suggest that different relations will be needed for different parts of the flow. Therefore, predicting the complete flow structures with global properties, whether β , $\Delta\beta$ or similar, currently appears not to be possible.

5 Conclusions

Flow field measurements taken using planar PIV have been presented of a TBL over a rough wall with different non-equilibrium PGs histories. Five strong PG histories are generated using a NACA0012 aerofoil of chord 1.25m. The flow fields captured focus on the region from one chord upstream of the leading edge to one chord downstream of the trailing edge. This region is particularly interesting since the wall pressure measurements show this to be the extent of the aerofoil's influence. The resulting flow fields are obtained at $12900 < Re_{\tau} < 18500$. It is seen that the strength of the pressure gradient has a clear relationship with the response time of the mean flow. This conclusion is based on the lag between β history and variation in Π . Extending previous work, it is seen that the optimum integration length is 1.17m or $6.4\delta_0$. This is much less than the previously used three chords in previous work. Furthermore, at larger values of $\Delta\beta$, the relationship with $\Delta\Pi$ is not linear as previously seen for lower values but is, in fact, 2nd-order. Examination of the mean turbulence profiles shows that matching $\Delta\beta$ allows for limited matching of the turbulence profiles. The agreement between matching $\Delta\beta$ is achieved if the local β value is similar. However, the matching of $\Delta\beta$ and local β is limited, and differences are seen in the profiles when different PG types are experienced. Quadrant analysis allowed the make-up of the Reynolds stresses to be analysed, particularly the contribution of sweeps and ejection events. At the edge of the log layer, FPGs increase the contribution of ejection events, while APGs have the opposite effect. The opposite trend is seen for sweep events, and under strong APGs, the contribution of sweep events overtakes that of ejection events. Higher up in the boundary layer, PGs are seen to have little effect on the contribution of the sweep events. PGs still affect ejection events, with FPGs reducing their contribution and APGs increasing it. Matching $\Delta \beta$ and β leads to similar distributions in the contribution of sweep and ejection events.

Two-point correlation allowed the response of the length scales and inclination of the structures within the flow to be examined. In agreement with previous works, FPGs lead to an increase in the streamwise length of the structures, and APGs lead to a reduction of both the small and large scales. Meanwhile, an APG leads to an increase in the inclination of the structures, while an FPG reduces it. The small scales within the flow show a faster response to the PG, especially for the inclination. Finally, the streamwise length of the structures was seen to increase further away from the wall where the structure is located. Further work is required to understand what other parameters, alongside $\Delta\beta$ are required to capture the variation in flow structures completely. Work is also needed to explore whether the relationships, especially for $\Delta\beta$, are surface and flow-independent. This requires more high-Reynolds data sets to examine what changes to the model are required to make it surface independent and universal to all flows.

A Comparison of PIV and HWA data at x/c = 2

To assess the spanwise uniformity of flow, the HWA and PIV profiles are compared, which are taken at two different spanwise coordinates. Both the HWA and PIV are taken within the central third of the wind tunnel. The HWA measurements are taken 0.45 m from the side wall, while the PIV data is taken more centrally, around 0.6 m from the side wall. As seen in figure 13a, there is good agreement between the HWA and PIV profiles in the outer region of the boundary layer in the mean velocity profile. Similar good agreement is seen in the mean streamwise Reynolds stress in figure 13b in the outer region. There are some small differences between the HWA and PIV analysis seen in the streamwise Reynolds stress; however, this is not a significant difference. These differences come from experimental uncertainty rather than spanwise variation of the flow.

Funding

We gratefully acknowledge the financial support from EPSRC (Grant Ref no: EP/W026090/1) and European Office for Airforce Research and Development (Grant No: FA8655-22-1-7163, Programme Manager: Dr. Doug Smith).

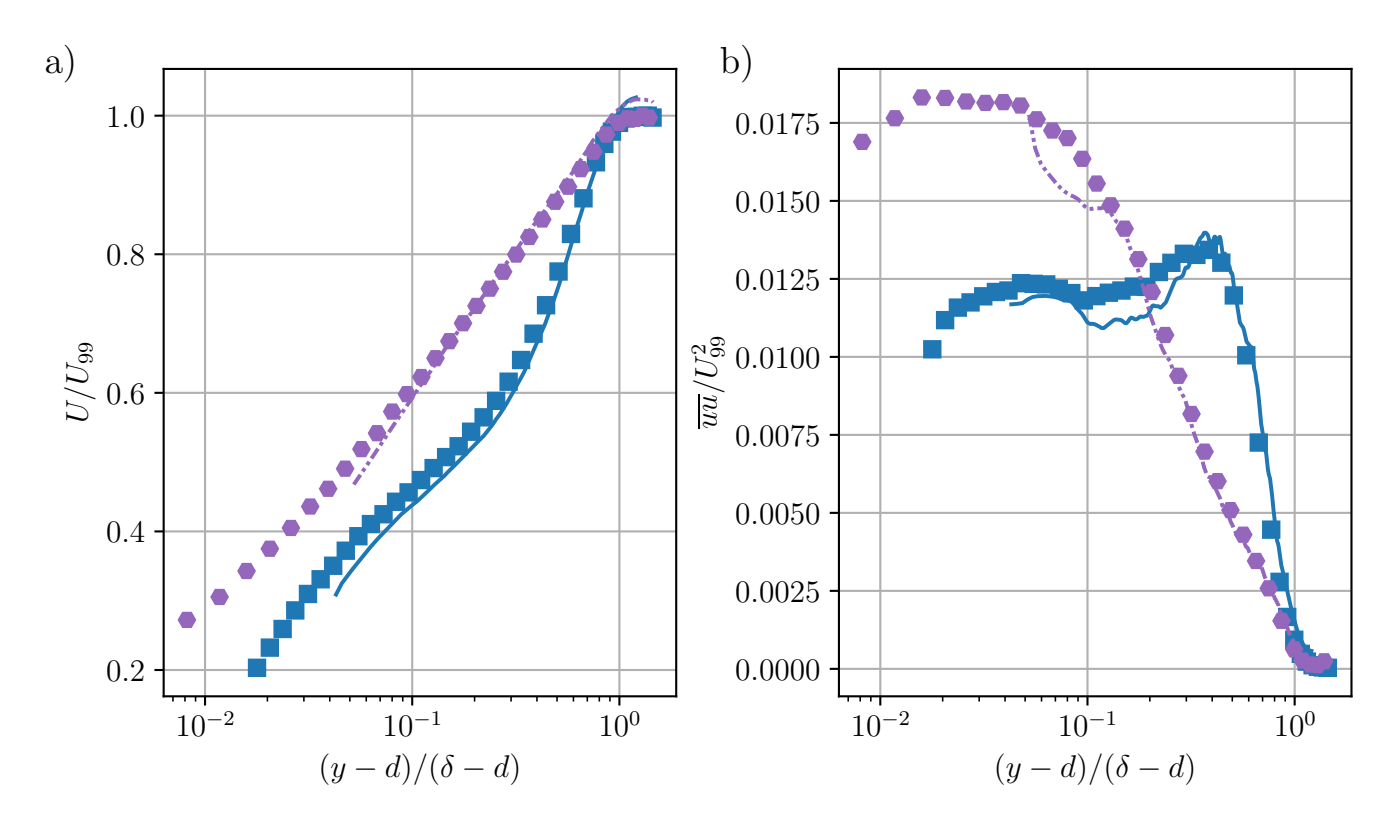


Figure 13: Comparison of boundary layer profiles at x/c=2 from HWA and PIV. (a) Shows variation in mean streamwise velocity normalised with boundary layer edge velocity and (b) shows the variation in mean streamwise Reynolds stress normalised with boundary layer edge velocity. HWA data shown by symbols and PIV shown by continuous lines as given in table 1.

Author contributions

TP designed the setup, conducted experiments, and post-processed PIV as well wrote the first draft. BG conceived the ideas for the experiment, acquired funding, edited drafts, and managed the project.

Data availability

Data published in this article is available on the University of Southampton repository (DOI: 10.5258/SOTON/D3530).

References

- A. Bobke, R. Vinuesa, R. Örlü, and P. Schlatter. History effects and near equilibrium in adverse-pressure-gradient turbulent boundary layers. *Journal of Fluid Mechanics*, 820:667–692, 2017.
- D. Chung, N. Hutchins, M.P. Schultz, and K.A. Flack. Predicting the drag of rough surfaces. *Annu. Rev. Fluid Mech.* 2021, 53:439–471, 2021.
- F.H. Clauser. Turbulent boundary layers in adverse pressure gradients. *Journal of the Aeronautical Sciences*, 21(2): 91–108, 1954.
- D. Coles. The law of the wake in the turbulent boundary layer. Journal of Fluid Mechanics, 1(2):191–226, 1956.
- W.J. Devenport and K.T. Lowe. Equilibrium and non-equilibrium turbulent boundary layers. Progress in Aerospace Sciences, 131:100807, 2022.
- M. Gul and B. Ganapathisubramani. Revisiting rough-wall turbulent boundary layers over sand-grain roughness. Journal of Fluid Mechanics, 911:A26, 2021.
- J. Jiménez. Turbulent flows over rough walls. Annual Review of Fluid Mechanics, 36:173–196, 2004.
- P.Å. Krogstad and P.E. Skåre. Influence of a strong adverse pressure gradient on the turbulent structure in a boundary layer. *Physics of Fluids*, 7(8):2014–2024, 1995.
- J.H. Lee. Large-scale motions in turbulent boundary layers subjected to adverse pressure gradients. Journal of Fluid Mechanics, 810:323–361, 2017.
- A. Lewkowicz. An improved universal wake function for turbulent boundary layers and some of its consequences. Z. Flugwiss. Weltraumforsch, 6:261–266, 1982.
- S.S. Lu and W.W. Willmarth. Measurements of the structure of the reynolds stress in a turbulent boundary layer. Journal of Fluid Mechanics, 60(3):481–511, 1973.
- I. Marusic, J.P. Monty, M. Hultmark, and A.J. Smits. On the logarithmic region in wall turbulence. *Journal of Fluid Mechanics*, 716:R3, 2013.
- J.P. Monty, N. Hutchins, H.C.H. Ng, I. Marusic, and M.S. Chong. A comparison of turbulent pipe, channel and boundary layer flows. *Journal of Fluid Mechanics*, 632:431–442, 2009.
- J.P. Monty, Z. Harun, and I. Marusic. A parametric study of adverse pressure gradient turbulent boundary layers. *International Journal of Heat and Fluid Flow*, 32(3):575–585, 2011.
- J. Nikuradse. Stromungsgesetze in rauhen rohren. vdi-forschungsheft, 361:1, 1933.
- T. Preskett, M. Virgilio, P. Jaiswal, and B. Ganapathisubramani. Effects of pressure-gradient histories on skin friction and mean flow of high reynolds number turbulent boundary layers over smooth and rough walls. *Journal of Fluid Mechanics*, 1010:A30, 2025.
- C. Sanmiguel Vila, R. Vinuesa, S. Discetti, A. Ianiro, P. Schlatter, and R. Örlü. Experimental realisation of near-equilibrium adverse-pressure-gradient turbulent boundary layers. Experimental Thermal and Fluid Science, 112: 109975, 2020.
- J.H. Shin and S.J. Song. Pressure gradient effects on smooth-and rough-surface turbulent boundary layers-part ii: Adverse pressure gradient. *Journal of Fluids Engineering, Transactions of the ASME*, 137(1):011204, 2015a.

- J.H. Shin and S.J. Song. Pressure gradient effects on smooth and rough surface turbulent boundary layers-part i: Favorable pressure gradient. *Journal of Fluids Engineering, Transactions of the ASME*, 137(1):011203, 2015b.
- G. Tay, D. Kuhn, and M. Tachie. Particle image velocimetry study of rough-wall turbulent flows in favorable pressure gradient. *Journal of fluids engineering*, 131(6):061205, 2009.
- J.M. Tsikata and M.F. Tachie. Adverse pressure gradient turbulent flows over rough walls. International Journal of Heat and Fluid Flow, 39:127–145, 2013.
- R. Vinuesa, A. Bobke, R. Örlü, and P. Schlatter. On determining characteristic length scales in pressure-gradient turbulent boundary layers. *Physics of Fluids*, 28(5):055101, 2016.
- R. Vinuesa, R. Örlü, C. Sanmiguel Vila, A. Ianiro, S. Discetti, and P. Schlatter. Revisiting history effects in adverse-pressure-gradient turbulent boundary layers. *Flow, Turbulence and Combustion*, 99(3):565–587, 2017.
- V. Vishwanathan, D.J. Fritsch, K.T. Lowe, and W.J. Devenport. History effects and wall-similarity of non-equilibrium turbulent boundary layers in varying pressure gradient over rough and smooth surfaces. *International Journal of Heat and Fluid Flow*, 102:109145, 2023.
- R.J. Volino. Non-equilibrium development in turbulent boundary layers with changing pressure gradients. *Journal of Fluid Mechanics*, 897:A2, 2020.
- R.J. Volino and M.P. Schultz. Comparison of smooth- and rough-wall non-equilibrium boundary layers with favourable and adverse pressure gradients. *Journal of Fluid Mechanics*, 959:A35, 2023.